

VALIDATION OF AN OPENFOAM[®]-BASED SOLVER FOR THE EULER EQUATIONS WITH BENCHMARKS FOR MESOSCALE ATMOSPHERIC MODELING

MICHELE GIRFOGLIO¹, ANNALISA QUAINI² AND GIANLUIGI ROZZA¹

ABSTRACT. Within OpenFOAM, we develop a pressure-based solver for the Euler equations written in conservative form using density, momentum, and total energy as variables. Under simplifying assumptions, these equations are used to describe non-hydrostatic atmospheric flow. For the stabilization of the Euler equations and to capture sub-grid processes, we consider two Large Eddy Simulation models: the classical Smagorinsky model and the one equation eddy-viscosity model. To achieve high computational efficiency, our solver uses a splitting scheme that decouples the computation of each variable. The numerical results obtained with our solver are validated against numerical data available in the literature for two classical benchmarks: the rising thermal bubble and the density current. Through qualitative and quantitative comparisons, we show that our approach is accurate. This work is meant to lay the foundation for a new open source package specifically created for quick assessment of new computational approaches for the simulation of atmospheric flows at the mesoscale level.

Keywords: Compressible flow, Low Mach number, Stratified flow, Non-hydrostatic atmospheric flows, Finite volume approximation, Large eddy simulation.

1. INTRODUCTION

Forecasting the rapid changes in the Earth's climate is one of the biggest challenges of our times. Since the complexity of the problem requires inputs and close collaboration from scientists across various disciplines, ranging from physics of the atmosphere to computer science, open source software has emerged as the obvious choice. In fact, the availability of open source software for use, modification, and distribution makes it ideal for collaborative development. Some examples of open source software for climate simulations are the Community Earth System Model [4], the Energy Exascale Earth System Model [5], the MIT General Circulation Model [7] and the Climate Machine [3]. All of these examples have large communities of active users and developers that have contributed over the course of several years. Since climate simulations are an extension of weather forecasting, we note that open source software has been a tool of choice for weather prediction as well. Examples include WRF [8] and Atlas [1].

Fast and accurate weather/climate forecasts need state-of-the-art numerical and computational methodologies. While the above mentioned software packages are great tools for realistic simulations, testing and assessing new numerical approaches within them is non-trivial. In fact, the very complexity that allows for realistic simulations requires a considerable amount of time to familiarize with, making such software impractical as testbed. This paper lays the foundation for a new open source package, called GEA (Geophysical and Environmental Applications) [6], specifically created for assessment of new computational approaches for the simulation of mesoscale atmospheric flows and ocean flows [21, 20]. That idea is that if a new approach fails to meet desired accuracy or efficiency standards in our simplified software, it would not be considered for implementation in more advanced software. To maximize the reach and impact, we choose to build our software package on OpenFOAM[®] [36], an open source, freely available C++ finite volume library that has become widely used in Computational Fluid Dynamics (CFD).

¹ MATHLAB, MATHEMATICS AREA, SISSA, VIA BONOMEA 265, I-34136 TRIESTE, ITALY

² DEPARTMENT OF MATHEMATICS, UNIVERSITY OF HOUSTON, HOUSTON TX 77204, USA

In recent years, OpenFOAM has been adopted to study a large variety of computational approaches for different CFD applications, including plasma cutting [22], fire plumes [27], and metal forming processes [32]. Thanks to parallel computing support, multiphase modeling capabilities, a wide range of existing turbulence models and ease of implementation for new ones, OpenFOAM represents a great tool for the development and assessment of computational strategies for atmospheric modeling. In this context, researchers have chosen OpenFOAM to perform atmospheric boundary layer simulations (see, e.g., [26, 12, 16]), multi-fluid atmospheric convection (see, e.g., [35]), mesh r -adaptivity for weather prediction over steep terrain (see, e.g., [37]). The results in [35, 37] have been obtained with AtmosFOAM [2], an OpenFOAM-based model of the global atmosphere using arbitrary shaped cells. Our solver starts with a focus on local atmospheric problem. However, we do not exclude interfacing it with AtmosFOAM in the future.

As the core of our open source package, we present an OpenFOAM-based solver for the Euler equations for stratified fluid flow, which are of importance in non-hydrostatic mesoscale atmospheric modeling, and assess it through two well-known test cases. We consider the Euler equations written in conservative form using density, momentum, and total energy as variables. It is shown in [17] that this set of equations yields less dissipative results than other forms of the Euler equations for relevant test problems. Hence, it was recommended to pursue this formulation for the development of mesoscale models despite the fact that other formulations (i.e., non-conservative forms and the conservative form using density, momentum, and potential temperature as variables) have received more attention for atmospheric studies. For the stabilization of the Euler equations and to capture sub-grid processes, we will assess and compare two Large Eddy Simulation (LES) models built in OpenFOAM: the classical Smagorinsky model [33] and the one equation eddy-viscosity model [38]. We will show that both LES models yield numerical results that agree very well with data published in the literature.

While nowadays both pressure-based and density-based approaches for the Euler equations are applicable to a wide range of flows, from incompressible to highly compressible, historically pressure-based solvers have been used for mildly compressible flows (as is the case for atmospheric flows). Despite this, the majority of the software for weather prediction adopts density-based approaches, which were originally designed for high-speed compressible flows. In this paper, we opt for a pressure-based solver and show that it yields accurate results when compared to data in the literature. In the spirit of OpenFOAM, our solver uses a splitting scheme that decouples the computation of each variable in order to achieve high computational efficiency.

The rest of the paper is organized as follows. In Sec. 2, we briefly describe the formulation of the Euler equations and the LES models under consideration. Sec. 3 presents our pressure-based approach and provides the details of space and time discretization. Numerical results for the two benchmark tests are discussed in Sec. 4. Conclusions are drawn in Sec. 5.

2. PROBLEM DEFINITION

2.1. The compressible Euler equations. We consider the dynamics of dry atmosphere in a spatial domain of interest Ω by neglecting the effects of moisture, solar radiation, and heat flux from the ground. We assume that dry air behaves like an ideal gas.

Let ρ be the air density, $\mathbf{u} = (u, v, w)$ the wind velocity, and e the total energy density. Note that $e = c_v T + |\mathbf{u}|^2/2 + gz$, where c_v the specific heat capacity at constant volume, T is the absolute temperature, g is the gravitational constant, and z is the vertical coordinate. The equations stating conservation of mass, momentum, and energy for the dry atmosphere written in terms of ρ , \mathbf{u} , and e over a time interval of interest $(0, t_f]$ read:

$$\begin{aligned}
 (1) \quad & \frac{\partial \rho}{\partial t} + \nabla \cdot (\rho \mathbf{u}) = 0 && \text{in } \Omega \times (0, t_f], \\
 (2) \quad & \frac{\partial(\rho \mathbf{u})}{\partial t} + \nabla \cdot (\rho \mathbf{u} \otimes \mathbf{u}) + \nabla p + \rho g \hat{\mathbf{k}} = \mathbf{0} && \text{in } \Omega \times (0, t_f], \\
 (3) \quad & \frac{\partial(\rho e)}{\partial t} + \nabla \cdot (\rho e \mathbf{u}) + \nabla \cdot (p \mathbf{u}) = 0 && \text{in } \Omega \times (0, t_f],
 \end{aligned}$$

where $\widehat{\mathbf{k}}$ is the unit vector aligned with the vertical axis z and p is pressure. To close system (1)-(3), we need a thermodynamics equation of state for p . Following the assumption that dry air behaves like an ideal gas, we have:

$$(4) \quad p = \rho RT,$$

where R is the specific gas constant of dry air.

Let us write the pressure as the sum of a fluctuation p' with respect to a background state

$$(5) \quad p = p' + \rho gz.$$

By plugging (5) into (2), we obtain:

$$(6) \quad \frac{\partial(\rho \mathbf{u})}{\partial t} + \nabla \cdot (\rho \mathbf{u} \otimes \mathbf{u}) + \nabla p' + gz \nabla \rho = 0 \quad \text{in } \Omega \times (0, t_f].$$

Let c_p be the specific heat capacity at constant pressure for dry air and let

$$(7) \quad K = |\mathbf{u}|^2/2, \quad h = c_v T + p/\rho = c_p T,$$

be the kinetic energy density and the specific enthalpy, respectively. The total energy density can be written as $e = h - p/\rho + K + gz$. Then, eq. (3) can be rewritten as:

$$(8) \quad \frac{\partial(\rho h)}{\partial t} + \nabla \cdot (\rho \mathbf{u} h) + \frac{\partial(\rho K)}{\partial t} + \nabla \cdot (\rho \mathbf{u} K) - \frac{\partial p}{\partial t} + \rho g \mathbf{u} \cdot \widehat{\mathbf{k}} = 0,$$

where we have used eq. (1) for further simplification. We will devise a splitting approach for problem (1),(4)-(8) because this formulation of the Euler equation facilitates the decoupling of all variables. In addition, it allows for an explicit treatment of the kinetic and potential energies.

Remark 2.1. *A quantity of interest for atmospheric problems is the potential temperature*

$$(9) \quad \theta = \frac{T}{\pi}, \quad \pi = \left(\frac{p}{p_0} \right)^{\frac{R}{c_p}},$$

i.e., the temperature that a parcel of dry air would have if it were expanded or compressed adiabatically to standard pressure $p_0 = 10^5$ Pa, which is the atmospheric pressure at the ground. Additionally, we define the potential temperature fluctuation θ' as the difference between θ and its mean hydrostatic value θ_0 :

$$(10) \quad \theta'(x, y, z, t) = \theta(x, y, z, t) - \theta_0(z).$$

Note that the hydrostatic reference state is a function of the vertical coordinate z only. See, e.g., [25] for more details.

2.2. LES models. The numerical discretization of the model presented in the previous subsection would lead to an accurate description of atmospheric flow if one could afford a discretization mesh able to capture all the scales of turbulent structures. Since the Kolmogorov scale of a typical atmospheric problem is about 10^{-4} m, a Direct Numerical Simulation is currently beyond reach. One way to keep the computational cost affordable is to solve for the flow average by using a coarser mesh and model the effects of the small scales that are not directly solved. This can be done via Large Eddy Simulation.

We will focus on two LES models: the classical Smagorinsky model [33] and the one equation eddy-viscosity model [38]. Both approaches are equivalent to introducing additional terms in eq. (6) and (8) of the form:

$$(11) \quad \frac{\partial(\rho \mathbf{u})}{\partial t} + \nabla \cdot (\rho \mathbf{u} \otimes \mathbf{u}) + \nabla p' + gz \nabla \rho - \nabla \cdot (2\mu_a \boldsymbol{\epsilon}(\mathbf{u})) + \nabla \cdot \left(\frac{2}{3} \mu_a \nabla \cdot \mathbf{u} \right) = 0 \quad \text{in } \Omega \times (0, t_f],$$

$$(12) \quad \frac{\partial(\rho h)}{\partial t} + \nabla \cdot (\rho \mathbf{u} h) + \frac{\partial(\rho K)}{\partial t} + \nabla \cdot (\rho \mathbf{u} K) - \frac{\partial p}{\partial t} + \rho g \mathbf{u} \cdot \widehat{\mathbf{k}} - \nabla \cdot \left(\frac{\mu_a}{Pr} \nabla h \right) = 0 \quad \text{in } \Omega \times (0, t_f],$$

where μ_a is an artificial viscosity, $\boldsymbol{\epsilon}(\mathbf{u}) = (\nabla \mathbf{u} + (\nabla \mathbf{u})^T)/2$ is the strain-rate tensor, and Pr is the Prandtl number, i.e., the dimensionless number defined as the ratio of momentum diffusivity to thermal diffusivity. The definition of μ_a is what distinguishes the different LES models.

The artificial dynamics viscosity, also called subgrid scale eddy viscosity, introduced by the Smagorinsky model is given by:

$$(13) \quad \mu_a = \rho(C_s \delta)^2 \sqrt{2\epsilon : \epsilon}, \quad C_s^2 = C_k \sqrt{\frac{C_k}{C_\epsilon}}$$

where δ is the filter width, and C_k and C_ϵ are model parameters. For the results in Sec. 4, we compute δ for each cell by taking the maximum distance between the cell center and a face center multiplied by 2. The main limitation of the Smagorinsky model lies in the assumption of local balance between the subgrid scale energy production and dissipation. The one equation eddy-viscosity model (kEqn model, for short) in [38] was developed to overcome this limitation. The artificial dynamics viscosity introduced by this model is given by:

$$(14) \quad \mu_a = \rho C_k \sqrt{k_{\text{sgs}}} \delta,$$

where C_k and δ represent the same quantities as in the Smagorinsky model and k_{sgs} is the subgrid scale kinetic energy computed from a transport equation that accounts for production, dissipation, and diffusion. See [38] for more details.

3. A SPLITTING APPROACH

This section presents a space and time discretization for the generic LES model (1),(4),(5),(7),(11), (12).

Let $\Delta t \in \mathbb{R}$, $t^n = n\Delta t$, with $n = 0, \dots, N_f$ and $t_f = N_f \Delta t$. Moreover, we denote by y^n the approximation of a generic quantity y at the time t^n . We adopt a Backward Differentiation Formula of order 1 (BDF1) for the discretization of the Eulerian time derivatives. Problem (1),(4),(5),(7),(11),(12) discretized in time reads: given ρ^0 , \mathbf{u}^0 , h^0 , p^0 , and T^0 , set $K^0 = |\mathbf{u}^0|^2/2$ and for $n \geq 0$ find solution $(\rho^{n+1}, \mathbf{u}^{n+1}, h^{n+1}, K^{n+1}, p^{n+1}, p'^{n+1}, T^{n+1})$ of system:

$$(15) \quad \frac{\rho^{n+1}}{\Delta t} + \nabla \cdot (\rho^{n+1} \mathbf{u}^{n+1}) = b_\rho^{n+1},$$

$$\frac{\rho^{n+1} \mathbf{u}^{n+1}}{\Delta t} + \nabla \cdot (\rho^{n+1} \mathbf{u}^{n+1} \otimes \mathbf{u}^{n+1}) + \nabla p'^{n+1} + gz \nabla \rho^{n+1}$$

$$(16) \quad - \nabla \cdot (2\mu_a^{n+1} \epsilon(\mathbf{u}^{n+1})) + \nabla \cdot \left(\frac{2}{3} \mu_a^{n+1} \nabla \cdot \mathbf{u}^{n+1} \right) = \mathbf{b}_\mathbf{u}^{n+1},$$

$$\frac{\rho^{n+1} h^{n+1}}{\Delta t} + \nabla \cdot (\rho^{n+1} \mathbf{u}^{n+1} h^{n+1}) + \frac{\rho^{n+1} K^{n+1}}{\Delta t} + \nabla \cdot (\rho^{n+1} \mathbf{u}^{n+1} K^{n+1})$$

$$(17) \quad - \frac{p^{n+1}}{\Delta t} + \rho^{n+1} g \mathbf{u}^{n+1} \cdot \hat{\mathbf{k}} - \nabla \cdot \left(\frac{\mu_a^{n+1}}{Pr} \nabla h^{n+1} \right) = b_e^{n+1},$$

$$(18) \quad p^{n+1} = p'^{n+1} + \rho^{n+1} gz,$$

$$(19) \quad p^{n+1} = \rho^{n+1} R T^{n+1},$$

$$(20) \quad h^{n+1} - h^n = c_p (T^{n+1} - T^n),$$

$$(21) \quad K^{n+1} = \frac{|\mathbf{u}^{n+1}|^2}{2},$$

where $b_\rho^{n+1} = \rho^n / \Delta t$, $\mathbf{b}_\mathbf{u}^{n+1} = \rho^n \mathbf{u}^n / \Delta t$, and $b_e^{n+1} = (\rho^n h^n + \rho^n K^n - p^n) / \Delta t$. Notice that in (20) we have chosen to update the value of the specific enthalpy in an incremental fashion.

A monolithic approach for coupled problem (15)-(21) would lead to high computational costs. Thus, to save computational time we adopt the following splitting approach: given ρ^0 , \mathbf{u}^0 , h^0 , p^0 and T^0 , set $K^0 = |\mathbf{u}^0|^2/2$ and for $n \geq 0$ perform

- Step 1: find first intermediate density $\rho^{n+\frac{1}{3}}$, intermediate velocity $\mathbf{u}^{n+\frac{1}{3}}$ and associated kinetic energy density $K^{n+\frac{1}{3}}$ such that

$$(22) \quad \frac{\rho^{n+\frac{1}{3}}}{\Delta t} = b_\rho^{n+1} - \nabla \cdot (\rho^n \mathbf{u}^n),$$

$$(23) \quad \frac{\rho^{n+\frac{1}{3}} \mathbf{u}^{n+\frac{1}{3}}}{\Delta t} + \nabla \cdot (\rho^n \mathbf{u}^n \otimes \mathbf{u}^{n+\frac{1}{3}}) + \nabla p^n - \nabla \cdot (2\mu_a^n \boldsymbol{\epsilon}(\mathbf{u}^{n+\frac{1}{3}})) + \nabla \left(\frac{2}{3} \mu_a^n \nabla \cdot \mathbf{u}^n \right) = \mathbf{b}_u^{n+1},$$

$$(24) \quad K^{n+\frac{1}{3}} = \frac{|\mathbf{u}^{n+\frac{1}{3}}|^2}{2}.$$

- Step 2: find specific enthalpy h^{n+1} , temperature T^{n+1} , and second intermediate density $\rho^{n+\frac{2}{3}}$ such that

$$(25) \quad \begin{aligned} & \frac{\rho^{n+\frac{1}{3}} h^{n+1}}{\Delta t} + \nabla \cdot (\rho^n \mathbf{u}^n h^{n+1}) - \nabla \cdot \left(\frac{\mu_a^n}{Pr} \nabla h^{n+1} \right) = \tilde{b}_e^n - \frac{\rho^{n+\frac{1}{3}} K^{n+\frac{1}{3}}}{\Delta t} \\ & - \nabla \cdot (\rho^n \mathbf{u}^n K^{n+\frac{1}{3}}) + \frac{p^n}{\Delta t} - \rho^{n+\frac{1}{3}} g \mathbf{u}^{n+\frac{1}{3}} \cdot \hat{\mathbf{k}}, \end{aligned}$$

$$(26) \quad h^{n+1} - c_p T^{n+1} = h^n - c_p T^n,$$

$$(27) \quad \rho^{n+\frac{2}{3}} R T^{n+1} = p^n,$$

where $\tilde{b}_e^n = (\rho^n h^n + \rho^n K^{n-1} - p^{n-1})/\Delta t$.

- Step 3: find end-of-step velocity \mathbf{u}^{n+1} and associated kinetic energy density K^{n+1} , pressure p^{n+1} and pressure fluctuation p'^{n+1} , and end-of-step density ρ^{n+1} such that

$$(28) \quad \frac{\rho^{n+\frac{1}{3}} \mathbf{u}^{n+1}}{\Delta t} + \nabla \cdot (\rho^n \mathbf{u}^n \otimes \mathbf{u}^{n+1}) + \nabla p^{n+1} - \nabla \cdot (2\mu_a^n \boldsymbol{\epsilon}(\mathbf{u}^{n+1})) + \nabla \left(\frac{2}{3} \mu_a^n \nabla \cdot \mathbf{u}^n \right) = \mathbf{b}_u^{n+1},$$

$$(29) \quad p^{n+1} - p'^{n+1} = \rho^{n+\frac{2}{3}} g z,$$

$$(30) \quad p^{n+1} - \rho^{n+1} R T^{n+1} = 0,$$

$$(31) \quad \frac{\rho^{n+\frac{2}{3}}}{\Delta t} + \nabla \cdot (\rho^{n+\frac{2}{3}} \mathbf{u}^{n+1}) = b_\rho^{n+1},$$

$$(32) \quad K^{n+1} = \frac{|\mathbf{u}^{n+1}|^2}{2}.$$

Notice that in eq. (28) one diffusive term is kept implicit, while the other is treated explicitly. This is customary in OpenFOAM.

The next section will describe the space discretization of the equations at each step and explain how to further reduce the computational cost associated with Step 3.

3.1. Space discretization. For the space discretization of (22)-(32), we adopt a finite volume method. This requires to partition the computational domain Ω into cells or control volumes Ω_i , with $i = 1, \dots, N_c$, where N_c is the total number of cells in the mesh. Let \mathbf{A}_j be the surface vector of each face of the control volume, with $j = 1, \dots, M$.

Let us start with Step 1. After applying the Gauss-divergence theorem, the integral form of eq. (22) for each volume Ω_i is given by:

$$(33) \quad \frac{1}{\Delta t} \int_{\Omega_i} \rho^{n+\frac{1}{3}} d\Omega = \int_{\Omega_i} b_\rho^{n+1} d\Omega - \int_{\partial\Omega_i} \rho^n \mathbf{u}^n \cdot d\mathbf{A}.$$

Let us denote with $(\rho^n \mathbf{u}^n)_i$ and $\rho_i^{n+\frac{1}{3}}$ the average flux and intermediate density in control volume Ω_i , respectively. Then, eq. (33) is approximated as follows:

$$(34) \quad \frac{1}{\Delta t} \rho_i^{n+\frac{1}{3}} + \sum_j \varphi_j^n = b_{\rho,i}^{n+1}, \quad \varphi_j^n = (\rho^n \mathbf{u}^n)_{i,j} \cdot \mathbf{A}_j,$$

where φ_j^n denotes the convective flux through face j of Ω_i and $b_{\rho,i}^{n+1}$ is the average right-hand side term in Ω_i . The convective flux at the cell faces is computed by a linear interpolation of the values from the adjacent cells.

Next, we consider eq. (23). Its integral form for each volume Ω_i , it is given by:

$$(35) \quad \frac{1}{\Delta t} \int_{\Omega_i} \rho^{n+\frac{1}{3}} \mathbf{u}^{n+\frac{1}{3}} d\Omega + \int_{\partial\Omega_i} \left(\rho^n \mathbf{u}^n \otimes \mathbf{u}^{n+\frac{1}{3}} \right) \cdot d\mathbf{A} + \int_{\Omega_i} \nabla p^n d\Omega \\ - \int_{\partial\Omega_i} 2\mu_a^n \boldsymbol{\epsilon}(\mathbf{u}^{n+\frac{1}{3}}) \cdot d\mathbf{A} + \int_{\partial\Omega_i} \left(\frac{2}{3} \mu_a^n \nabla \cdot \mathbf{u}^n \right) d\mathbf{A} = \int_{\Omega_i} \mathbf{b}_{\mathbf{u}}^{n+1} d\Omega,$$

after the application of the Gauss-divergence theorem. For the approximation of most of the terms in (35), we follow [19]. So, we write the discretized form of (35) divided by the control volume Ω_i as:

$$(36) \quad \frac{1}{\Delta t} \rho_i^{n+\frac{1}{3}} \mathbf{u}_i^{n+\frac{1}{3}} + \sum_j \varphi_j^n \mathbf{u}_{i,j}^{n+\frac{1}{3}} + \nabla p_i^n - \sum_j 2\mu_a^n \boldsymbol{\epsilon}(\mathbf{u}_i^{n+\frac{1}{3}})_j \cdot \mathbf{A}_j \\ + \sum_j \left(\frac{2}{3} \mu_a^n (\nabla \cdot \mathbf{u}^n)_j \right) \mathbf{A}_j = \mathbf{b}_{\mathbf{u},i}^{n+1},$$

where $\mathbf{u}_i^{n+\frac{1}{3}}$, p_i^n , and $\mathbf{b}_{\mathbf{u},i}^{n+1}$ are the average intermediate velocity, pressure, and source term in control volume Ω_i , while $\mathbf{u}_{i,j}^{n+\frac{1}{3}}$ denotes the intermediate velocity associated to the centroid of face j normalized by the volume of Ω_i . This approximation of $\mathbf{u}^{n+\frac{1}{3}}$ at cell face j is obtained with a third order interpolation scheme [36]. We will use the same scheme for all the flux terms in the equations below. For term $\boldsymbol{\epsilon}(\mathbf{u}_i^{n+\frac{1}{3}})_j$, we need to approximate the gradient of $\mathbf{u}_i^{n+\frac{1}{3}}$ at face j . We choose to do it with second order accuracy. See [24] for more details. The pressure term is treated with a second-order face flux reconstruction in order to suppress spurious oscillations [9]. We discretize all the pressure terms in the following equations in the same way.

To complete Step 1, we need the discretized form of eq. (24), which is given by

$$(37) \quad K_i^{n+\frac{1}{3}} = \frac{|\mathbf{u}_i^{n+\frac{1}{3}}|^2}{2}.$$

Let us now consider Step 2. After the application of the Gauss-divergence theorem, the integral form of eq. (25) for each volume Ω_i becomes:

$$(38) \quad \frac{1}{\Delta t} \int_{\Omega_i} \rho^{n+\frac{1}{3}} h^{n+1} d\Omega + \int_{\partial\Omega_i} (\rho^n \mathbf{u}^n h^{n+1}) \cdot d\mathbf{A} - \int_{\partial\Omega_i} \left(\frac{\mu_a^n}{Pr} \nabla h^{n+1} \right) \cdot d\mathbf{A} = \int_{\Omega_i} \tilde{b}_e^n d\Omega \\ - \frac{1}{\Delta t} \int_{\Omega_i} \rho^{n+\frac{1}{3}} K^{n+\frac{1}{3}} d\Omega - \int_{\partial\Omega_i} (\rho^n \mathbf{u}^n K^{n+\frac{1}{3}}) \cdot d\mathbf{A} + \frac{1}{\Delta t} \int_{\Omega_i} p^n d\Omega - \int_{\Omega_i} \rho^{n+\frac{1}{3}} g \mathbf{u}^{n+\frac{1}{3}} \cdot \hat{\mathbf{k}} d\Omega,$$

The discretized form of eq. (38) can be written as:

$$(39) \quad \frac{1}{\Delta t} \rho_i^{n+\frac{1}{3}} h_i^{n+1} + \sum_j \varphi_j^n h_{i,j}^{n+1} - \sum_j \frac{\mu_a}{Pr} (\nabla h_i^{n+1})_j \cdot \mathbf{A}_j = \tilde{b}_{e,i}^n \\ - \frac{1}{\Delta t} \rho_i^{n+\frac{1}{3}} K_i^{n+\frac{1}{3}} - \sum_j \varphi_j^n K_{i,j}^{n+\frac{1}{3}} + \frac{1}{\Delta t} p_i^n - \rho_i^{n+\frac{1}{3}} g \mathbf{u}_i^{n+\frac{1}{3}} \cdot \hat{\mathbf{k}},$$

where h_i^{n+1} and $b_{e,i}^n$ are the average specific enthalpy and source term in control volume Ω_i , while $h_{i,j}^{n+1}$ and $K_{i,j}^{n+\frac{1}{3}}$ denote the specific enthalpy and kinetic energy density associated to the centroid of face j normalized by the volume of Ω_i . Finally, $(\nabla h_i^{n+1})_j$ is the gradient of h_i^{n+1} at face j .

To complete Step 2, we need the discretized form of eqs. (26) and (27), which are given by

$$(40) \quad h_i^{n+1} - c_p T_i^{n+1} = h_i^n - c_p T_i^n,$$

$$(41) \quad \rho_i^{n+\frac{2}{3}} R T_i^{n+1} = p_i^n.$$

Note that the specific enthalpy is computed from eq. (39), so one computes the end-of-step temperature from (40) and the second intermediate density from (41) in a completely decoupled fashion.

The treatment of Step 3 requires careful attention in order to contain the computational cost. We start by plugging eq. (29) into eq. (28). The integral form of the resulting equation for each volume Ω_i is given by:

$$(42) \quad \frac{1}{\Delta t} \int_{\Omega_i} \rho^{n+\frac{1}{3}} \mathbf{u}^{n+1} d\Omega + \int_{\partial\Omega_i} (\rho^n \mathbf{u}^n \otimes \mathbf{u}^{n+1}) \cdot d\mathbf{A} + \int_{\Omega_i} \nabla p'^{n+1} d\Omega + \int_{\Omega_i} gz \nabla \rho^{n+\frac{2}{3}} d\Omega \\ - \int_{\partial\Omega_i} 2\mu_a^n \boldsymbol{\epsilon}(\mathbf{u}^{n+1}) \cdot d\mathbf{A} + \int_{\partial\Omega_i} \left(\frac{2}{3} \mu_a^n \nabla \cdot \mathbf{u}^n \right) d\mathbf{A} = \int_{\Omega_i} \mathbf{b}_{\mathbf{u}}^{n+1} d\Omega,$$

after the application of the Gauss-divergence theorem. Each term in (42) is approximated like the corresponding term in (35). Hence, the discretized form of (42), divided by the control volume Ω_i , is given by:

$$(43) \quad \frac{1}{\Delta t} \rho_i^{n+\frac{1}{3}} \mathbf{u}_i^{n+1} + \sum_j \varphi_j^n \mathbf{u}_{i,j}^{n+1} + \nabla p_i'^{n+1} + gz_i \nabla \rho_i^{n+\frac{2}{3}} \\ - \sum_j 2\mu_a^n \boldsymbol{\epsilon}(\mathbf{u}_i^{n+1})_j \cdot \mathbf{A}_j + \sum_j \left(\frac{2}{3} \mu_a^n (\nabla \cdot \mathbf{u}^n)_j \right) \mathbf{A}_j = \mathbf{b}_{\mathbf{u},i}^{n+1},$$

where \mathbf{u}_i^{n+1} , $p_i'^{n+1}$ and $\mathbf{b}_{\mathbf{u},i}^{n+1}$ are the average end-of-step velocity, pressure fluctuation, and source term in control volume Ω_i , while $\mathbf{u}_{i,j}^{n+1}$ denotes the end-of-step velocity associated to the centroid of face j normalized by the volume of Ω_i . In (43), z_i is the vertical coordinate of the centroid of cell Ω_i .

Following [24], we now write eq. (43) in semi-discretized form, i.e., with some terms in continuous form while all other terms (grouped in \mathbf{H}) are in discrete form:

$$(44) \quad \mathbf{u}^{n+1} = \frac{\Delta t}{\rho^{n+\frac{1}{3}}} \left(\mathbf{H}(\mathbf{u}_i^{n+1}) - gz \nabla \rho^{n+\frac{2}{3}} - \nabla p'^{n+1} \right), \\ \mathbf{H}(\mathbf{u}_i^{n+1}) = - \sum_j \varphi_j^n \mathbf{u}_{i,j}^{n+1} + \sum_j 2\mu_a^n \boldsymbol{\epsilon}(\mathbf{u}_i^{n+1})_j \cdot \mathbf{A}_j - \sum_j \left(\frac{2}{3} \mu_a^n (\nabla \cdot \mathbf{u}^n)_j \right) \mathbf{A}_j + \mathbf{b}_{\mathbf{u},i}^{n+1}.$$

Next, we plug (44) into (31) to obtain:

$$(45) \quad \frac{1}{\Delta t} \rho^{n+\frac{2}{3}} + \nabla \cdot \left(\rho^{n+\frac{2}{3}} \left(\frac{\Delta t}{\rho^{n+\frac{1}{3}}} \left(\mathbf{H}(\mathbf{u}^{n+1}) - gz \nabla \rho^{n+\frac{2}{3}} - \nabla p'^{n+1} \right) \right) \right) = b_{\rho}^{n+1}.$$

By integrating eq. (45) over the control volume Ω_i , applying the Gauss-divergence theorem, and dividing by the control volume, we get:

$$(46) \quad \sum_j \rho_j^{n+\frac{2}{3}} (\nabla p_i'^{n+1})_j \cdot \mathbf{A}_j = \sum_j \frac{\rho_j^{n+\frac{2}{3}} \Delta t}{\rho_j^{n+\frac{1}{3}}} \left(\mathbf{H}(\mathbf{u}_i^{n+1})_j - gz_j (\nabla \rho_i^{n+\frac{2}{3}})_j \right) \cdot \mathbf{A}_j - b_{\rho,i}^{n+1} + \frac{1}{\Delta t} \rho_i^{n+\frac{2}{3}},$$

which is used to compute the pressure fluctuation. In eq. (46), $(\nabla p_i'^{n+1})_j$ and $(\nabla \rho_i^{n+\frac{2}{3}})_j$ are the gradients of p'^{n+1} and $\rho_i^{n+\frac{2}{3}}$ at faces j , respectively. In OpenFOAM, there are a few partitioned algorithms that decouple the computation of the pressure from the computation of the velocity, namely SIMPLE [31] for steady-state problems, PISO [23] and PIMPLE [30] for time-dependent problems. In this work, we use the PISO algorithm.

Now that we have computed the pressure fluctuation and the end-of-step velocity, we can get the pressure and the end-of-step kinetic energy density using the discretized forms of (29) and (32):

$$p_i^{n+1} = p_i'^{n+1} + \rho_i^{n+\frac{2}{3}} gz_i, \\ K_i^{n+1} = \frac{|\mathbf{u}_i^{n+1}|^2}{2}.$$

Finally, we compute the end-of-step density with the space-discrete version of eq. (30):

$$(47) \quad \rho_i^{n+1} = \frac{p_i^{n+1}}{RT_i^{n+1}}.$$

4. NUMERICAL RESULTS

We test our OpenFOAM-based solver for the Euler equation with two standard benchmarks that have been widely used to assess atmospheric dynamical cores, i.e., the rising thermal bubble and the density current. Both test cases involve a perturbation of a neutrally stratified atmosphere with uniform background potential temperature over a flat terrain. So, before reporting the results for the two benchmarks, in Sec. 4.1 we show that an unperturbed stratified atmosphere with uniform background potential temperature over a flat terrain remains unchanged up to a certain tolerance. In Sec. 4.2 we present our results for the rising thermal bubble benchmark. There exist several variations of this benchmark, featuring different geometries and/or initial conditions. We use the settings from [10]. See also [15] for a recent work using this variation. Our results for the classical density current test [14, 34] are shown in Sec. 4.3. We would like to point out that neither the rising bubble nor the density current benchmark has an exact solution. Hence, one can only have a relative comparison with other numerical data available in the literature.

4.1. Hydrostatic atmosphere. The goal of this first test case is to verify that an initial resting atmosphere over a flat terrain remains still within a reasonable accuracy for a long time interval.

The computational domain in the xz -plane is $\Omega = [0, 16000] \times [0, 800]$ m². In this domain, the hydrostatic atmosphere, initially at rest, is free to evolve until $t = 25$ days [13]. Impenetrable, free-slip boundary conditions are imposed at all the boundaries. We consider a uniform mesh with mesh sizes $h = \Delta x = \Delta z = 250$ m and we set the time step to $\Delta t = 0.1$ s.

Figure 1 shows the time evolution of the maximal vertical velocity w_{max} . We observe that w_{max} has an initial, rather fast, growth but subsequently stabilizes around $1e-5$ m/s. Thus, we conclude that the hydrostatic equilibrium is preserved with reasonably good accuracy, especially in view of the two benchmarks we are going to study next.

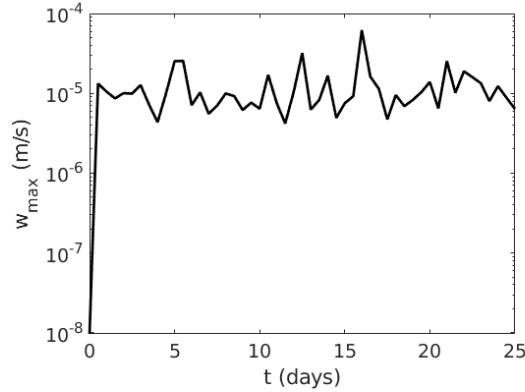


FIGURE 1. Hydrostatic atmosphere: time evolution of the maximal vertical velocity w_{max} .

4.2. Rising thermal bubble in a neutrally stratified atmosphere. The computational domain in the xz -plane is $\Omega = [0, 5000] \times [0, 10000]$ m² and the time interval of interest is $(0, 1020]$ s. Impenetrable, free-slip boundary conditions are imposed on all walls. The initial density is given by

$$(48) \quad \rho^0 = \frac{p_g}{R\theta_0} \left(\frac{p}{p_g} \right)^{c_v/c_p}, \quad p = p_g \left(1 - \frac{gz}{c_p\theta_0} \right)^{c_p/R},$$

with $c_p = R + c_v$, $c_v = 715.5 \text{ J}/(\text{Kg K})$, $R = 287 \text{ J}/(\text{Kg K})$. In (48), θ^0 is the initial potential temperature, which is defined as:

$$(49) \quad \theta^0 = 300 + 2 \left[1 - \frac{r}{r_0} \right] \text{ if } r \leq r_0 = 2000 \text{ m, } \theta^0 = 300 \text{ otherwise,}$$

where $r = \sqrt{(x - x_c)^2 + (z - z_c)^2}$, $(x_c, z_c) = (5000, 2000) \text{ m}$ [10, 11]. Notice that (48)-(49) represents a neutrally stratified atmosphere with uniform background potential temperature of 300 K perturbed by a circular bubble of warmer air. The initial velocity field is zero everywhere. Finally, the initial specific enthalpy is given by:

$$(50) \quad h^0 = c_p \theta^0 \left(\frac{p}{p_g} \right)^{\frac{R}{c_p}}.$$

For this test, we use five different meshes with uniform resolution $h = \Delta x = \Delta z = 250, 125, 62.5, 31.25, 15.625 \text{ m}$. The time step is set to $\Delta t = 0.1 \text{ s}$ for all the simulations. For stabilization, we consider two strategies. First, following [10], we set $\mu_a = 15$ and $Pr = 1$. Note that while $Pr = 1$ is close to a physically meaningful value as the air Prandtl number is about 0.71 at 20°C, $\mu_a = 15$ is an ah-hoc value. Hereinafter, we refer to this model as AV15, where AV stands for artificial viscosity. Then, we consider the Smagorinsky model as described in Sec. 2.2.

Figure 2 reports the perturbation of potential temperature θ' at $t = 1020 \text{ s}$ computed by the AV15 model with all the meshes under consideration. By $t = 1020$, the air warmer than the ambient has risen due to buoyancy and deformed due to shearing motion. As a result, the bubble has evolved into a mushroom shape. From Figure 2, we observe that there is no substantial change in the computed θ' when the mesh is refined past $h = 125 \text{ m}$. We remark that, to facilitate the comparison of the panels in Figure 2, we have forced the colorbar to range from 0 to 1. Qualitatively, these results are in very good agreement with those reported in the literature. See, e.g., [10, 11, 29].

For further qualitative assessment, Figure 3 displays velocity components u and w at $t = 1020 \text{ s}$ computed by the AV15 model with mesh $h = 125 \text{ m}$. These contour plots are in very good agreement with those reported in the literature. See, e.g., Figure 7 in [10].

For a more quantitative comparison, in Figure 4 we show the time evolution of the maximum perturbation of potential temperature θ'_{max} and maximum vertical component of the velocity w_{max} computed by the AV15 model with all the meshes, together with the corresponding results from [10]. We observe that the evolution of θ'_{max} computed with meshes $h = 250 \text{ m}$ and $h = 125 \text{ m}$ is affected by spurious oscillations. Such oscillation disappears at higher resolution and they are not present at all in the evolution of w_{max} . We see that θ'_{max} and w_{max} computed with meshes $h = 31.25 \text{ m}$ and $h = 15.625 \text{ m}$ are practically overlapped for the entire time interval, indicating that we are close to convergence. The “converged” w_{max} overlaps with the reference value till about $t = 500 \text{ s}$ and it remains close to it till about $t = 800 \text{ s}$. The agreement of the “converged” θ'_{max} with the results from [10] is not as good. These trends are confirmed from Table 1, which reports the extrema for the vertical velocity w and potential temperature perturbation θ' at $t = 1020 \text{ s}$ obtained with the AV15 model, together with the values extracted from the figures in [10]. The results from [10] are obtained with mesh resolution of 125 m and a density-based approach developed from a Godunov-type scheme that employs flux-based wave decompositions for the solution of Riemann problem. The authors of [10] start from the Euler equations written in density, velocity, and potential temperature. Other differences with our methodology include the orders of space and time discretizations and the different treatment of the hydrostatic term. Given all these differences, we believe that our results cannot be considered off with respect to the reference. In addition, other references, such as [29] (see Fig. 1, top left panel), report a θ'_{max} at $t = 1020 \text{ s}$ computed with resolution 125 m closer to 1K (like in our case) than to 1.4 K (like in [10]).

Finally, we run this test with the Smagorinsky model. We set the parameter $C_s = 0.094$, with $C_k = 0.21$ and $C_\epsilon = 1.048$. Details on the choice of these parameters are reported in Sec. 4.3. Figure 5 depicts the spatial distribution of θ' at $t = 1020 \text{ s}$ computed with meshes 15.625 m and 32.25 m. As expected, with these fine meshes the Smagorinsky model is able to capture a larger amount of vortical structures than the AV15 model. The beautiful vortex strip created by the Rayleigh-Taylor

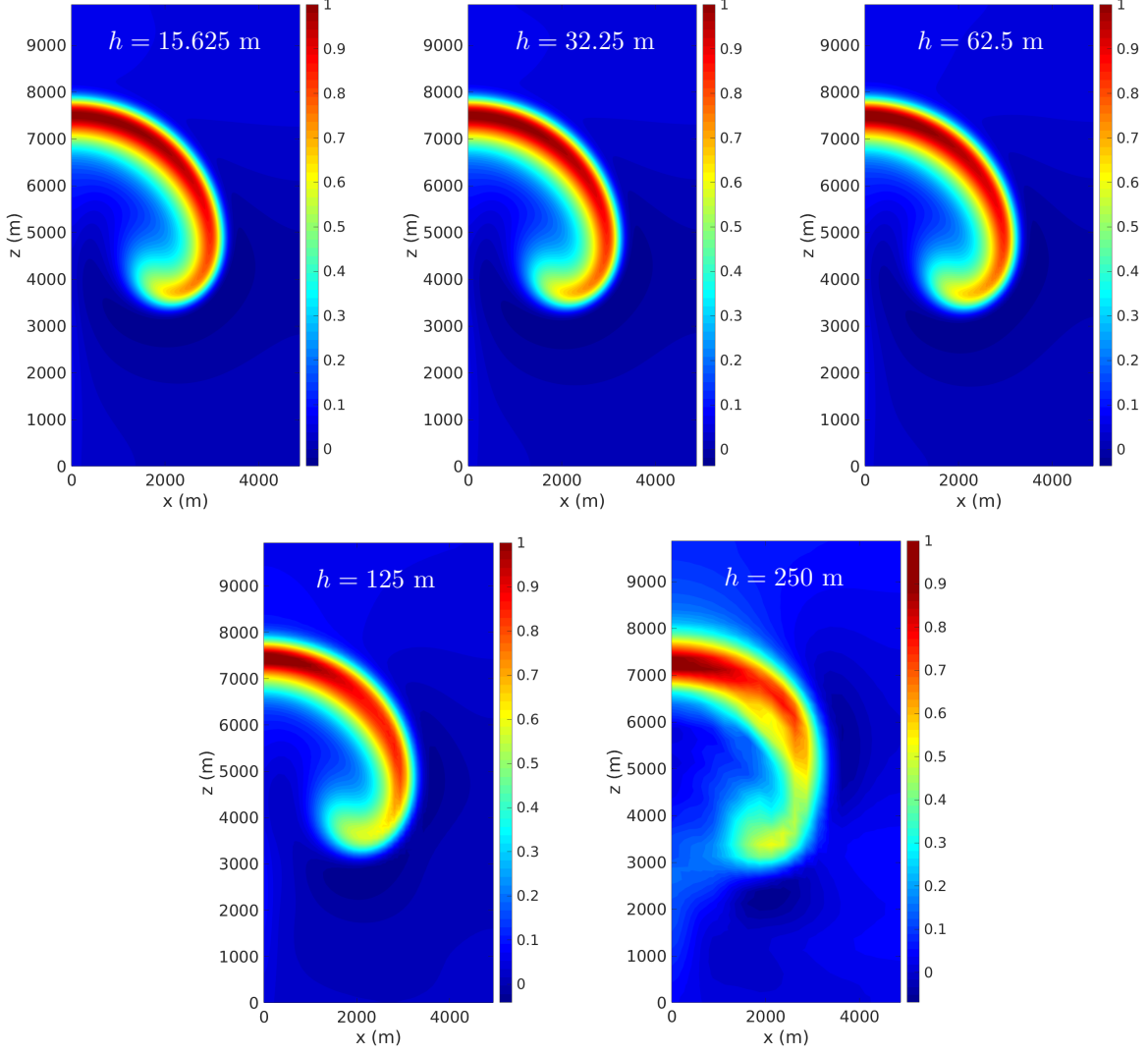


FIGURE 2. Rising thermal bubble, AV15 model: perturbation of potential temperature computed with mesh $h = 15.625$ m (top-left), $h = 32.25$ m (top-center), $h = 62.5$ m (top-right), $h = 125$ m (bottom-left), $h = 250$ m (bottom-right)

Model	Resolution [m]	w_{min} (m/s)	w_{max} (m/s)	θ'_{min} (K)	θ'_{max} (K)
AV15	15.625	-10.02	12.17	-0.038	1
AV15	31.25	-10.05	12.13	-0.037	1.01
AV15	62.5	-10.08	12.09	-0.037	1.03
AV15	125	-10.02	11.97	-0.042	1.06
AV15	250	-9.59	11.23	-0.069	0.89
Ref. [10]	125	-7.75	13.95	-0.01	1.4

TABLE 1. Rising thermal bubble, AV15 model: minimum and maximum vertical velocity w and potential temperature perturbation θ' at $t = 1020$ s compared with the values extracted from the figures in [10].

instability at the edge of the bubble shown in Figure 5 (left) matches well with that shown in [29] (see Fig. 1, bottom right panel). Table 2 reports the extrema for the vertical velocity w and potential

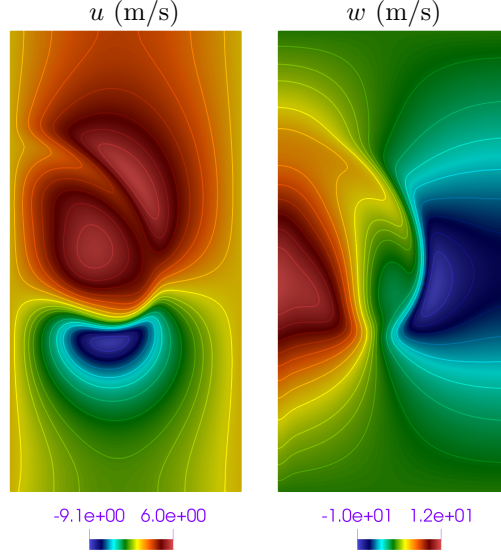


FIGURE 3. Rising thermal bubble, AV15 model: contour plots of the horizontal velocity component u (left) and the vertical velocity component w (right) at $t = 1020$ s computed with mesh $h = 125$ m.

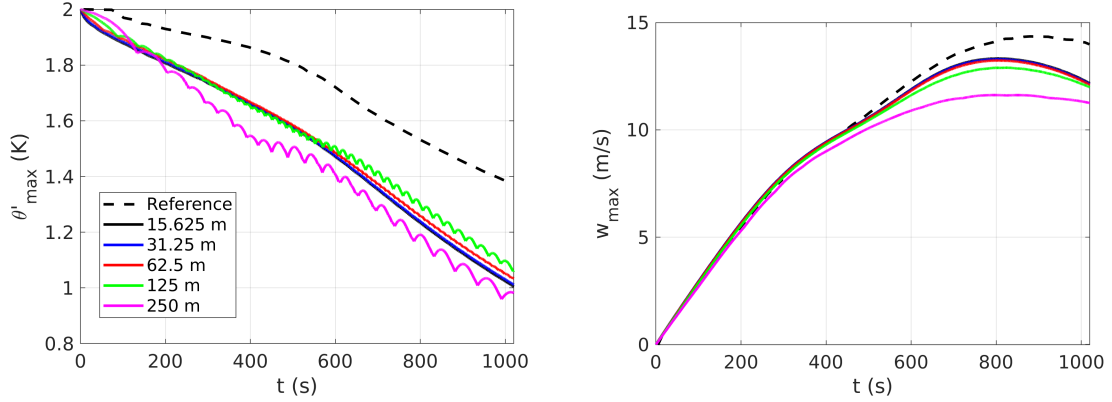


FIGURE 4. Rising thermal bubble, AV15 model: time evolution of the maximum perturbation of potential temperature θ'_{max} (left) and the maximum vertical component of the velocity w_{max} (right) computed with all the meshes under consideration. The reference values are taken from [10] and refer to resolution 125 m.

temperature perturbation θ' at $t = 1020$ s obtained with the Smagorinsky model. Since we could not find any data obtained with a LES model for the exact setting of [10], Table 2 does contain reference data for comparison.

Model	Resolution [m]	w_{min} (m/s)	w_{max} (m/s)	θ'_{min} (K)	θ'_{max} (K)
Smagorinsky (LES)	15.625	-12.24	15.42	-0.18	2.04
Smagorinsky (LES)	31.25	-11.54	15.04	-0.072	1.89

TABLE 2. Rising thermal bubble, Smagorinsky model: minimum and maximum vertical velocity w and potential temperature perturbation θ' at $t = 1020$ s.

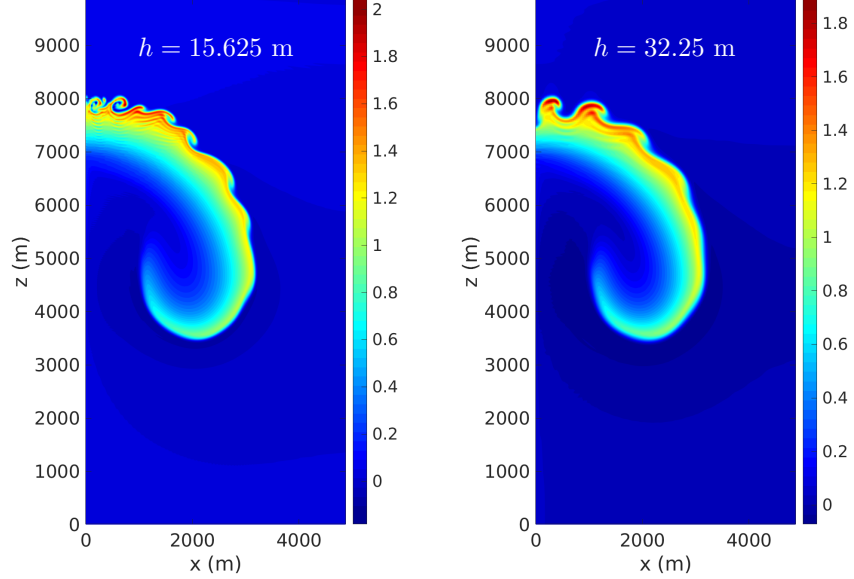


FIGURE 5. Rising thermal bubble, Smagorinsky model: perturbation of potential temperature computed with mesh $h = 15.625$ m (left) and $h = 32.25$ m (right).

4.3. Density current. The computational domain in the xz -plane is $\Omega = [0, 25600] \times [0, 6400]$ m² and the time interval of interest is $(0, 900]$ s. Impenetrable, free-slip boundary conditions are imposed on all the walls. The initial density is given by (48) with initial potential temperature:

$$(51) \quad \theta^0 = 300 - \frac{15}{2} [1 + \cos(\pi r)] \text{ if } r \leq 1, \quad \theta^0 = 300 \text{ otherwise,}$$

where $r = \sqrt{\left(\frac{x-x_c}{x_r}\right)^2 + \left(\frac{z-z_c}{z_r}\right)^2}$, with $(x_r, z_r) = (4000, 2000)$ m and $(x_c, z_c) = (0, 3000)$ m. The initial potential temperature fluctuation (10) on part of the domain Ω is shown in Fig. 6. Notice that in this case the initial bubble is cold, while the bubble in (49) is warm. The initial velocity field is zero everywhere and the initial specific enthalpy is given by (50).

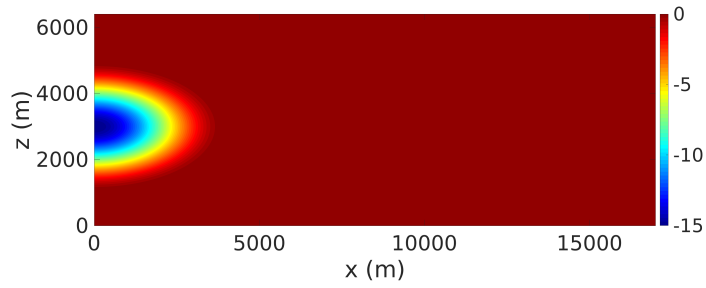


FIGURE 6. Density current: initial potential temperature fluctuation θ' on part of the computational domain.

We first consider uniform meshes with commonly used [34, 10, 18, 28, 29] mesh sizes $h = \Delta x = \Delta z = [400, 200, 100, 50, 25]$ m. The time step is set to $\Delta t = 0.1$ s. Since this benchmark features more complex vortical structures than the rising thermal bubble, we consider three stabilization strategies. Following [34, 10] we first set $\mu_a = 75$ in (11)-(12) and $Pr = 1$ in (12). We will refer to this model as AV75, since 75 is an ad-hoc artificial value. Then, we consider the Smagorinsky and the kEqn models as described in Sec. 2.2.

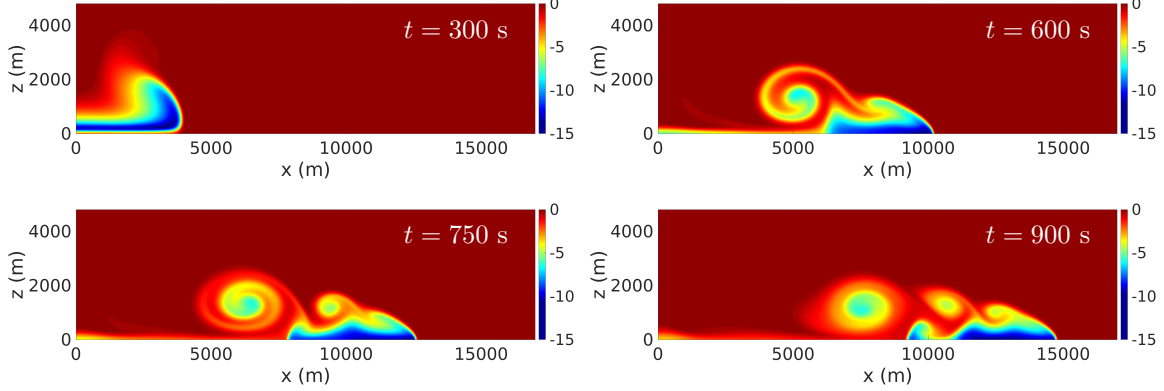


FIGURE 7. Density current, AV75 model: time evolution of potential temperature fluctuation θ' computed with mesh $h = 25$ m.

Let us start with the AV75 model and a qualitative illustration of the flow evolution. Figure 7 shows θ' computed with the AV75 model and mesh $h = 25$ m (i.e., the finest mesh among those considered) at $t = 300, 600, 750, 900$ s. We observe very good agreement with the results reported in Fig. 1 of [34], which were obtained with the same resolution. Indeed, we see that, as expected, the cold air descends due to negative buoyancy and strong downdrafts develop at the center of the cold bubble. When the cold air reaches the ground, it rolls up and forms a front. As this front propagates, shear is generated at its top boundary with a resulting Kelvin-Helmholtz type instability that leads to a three-rotor structure at $t = 900$ for the resolution under consideration.

In Figure 8, we report θ' computed at $t = 900$ s by the AV75 model with all the meshes mentioned above. We observe the emergence of a clear three-rotor structure when the resolution is equal to or smaller than $h = 100$ m, with more definition when the mesh is finer. Also the results in Figure 8 are in very good agreement with those reported in the literature. See, e.g., [34, 10, 18, 28, 29].

Next, we focus on the Smagorinsky model. Given the poor quality of the solutions computed with the AV75 model and meshes coarser than $h = 100$ m, we will use only the meshes finer than $h = 100$ m. Moreover, following [29] for the LES models we will also consider a very fine mesh with size $h = 12.5$ m. Figures 9, 10, and 11 display the time evolution of the potential temperature fluctuation computed with the Smagorinsky model and meshes $h = 12.5, 25, 50$ m, respectively. For all these simulations, the parameter C_s (13) was set to 0.454, with $C_k = 0.6$ and $C_\epsilon = 1.048$. We note that the ratio of the values of C_s used for this benchmark and for the rising thermal bubble is about 5, which is the ratio of the ad-hoc artificial viscosities. From Figures 9-11, we clearly see that more vortical structures appear as the mesh size decreases. Indeed, we can see what while with $h = 50$ m there is a three-rotor structure at $t = 900$ s (see Fig. 11, bottom right panel), with $h = 25$ m a quadri-rotor structure is present (see Fig. 10, bottom right panel). The largest recirculation in the bottom right panels of 11 and 10 is broken into two recirculations when mesh $h = 12.5$ m is used. See Fig. 9, bottom right panel.

To further justify our choice of C_s , we report in Figure 12 the time evolution of the space-averaged eddy viscosity

$$(52) \quad \mu_{av} = \frac{1}{\Omega} \int_{\Omega} \mu_a d\Omega$$

for meshes $h = 12.5, 25, 50$ m. We see that μ_{av} decreases with increasing resolution over most of the time interval. This is expected since the eddy viscosity (13) is a quadratic function of the filter width, which is related to the mesh size. However, even with the coarsest mesh (i.e., $h = 50$ m), the space-averaged eddy viscosity is much smaller than 75, i.e., the value used by the AV75 model. Values of C_s smaller than 0.454 do not provide enough artificial dissipation to stabilize the solution, leading to under-resolved regions and a significant amount of noise above the recirculations. The

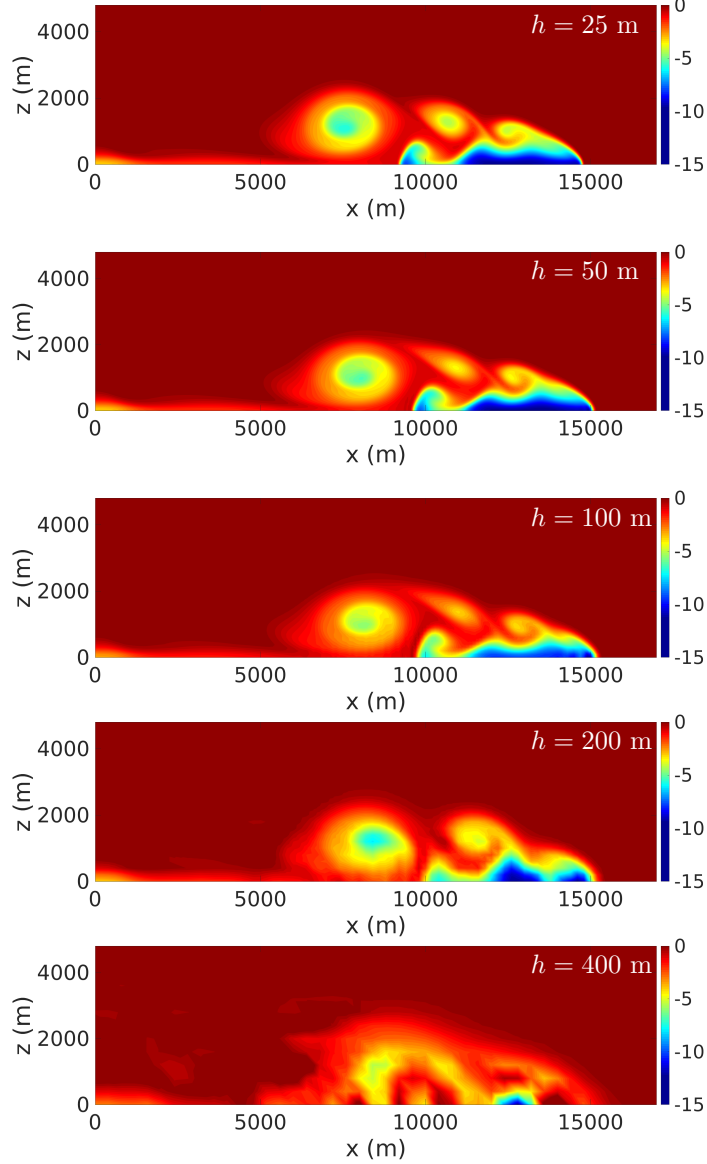


FIGURE 8. Density current, AV75 model: potential temperature fluctuation θ' computed at $t = 900$ s with meshes $h = 25, 50, 100, 200, 400$ m. The mesh size is increasing from top to bottom.

value $C_s = 0.454$ ensures a good compromise between accuracy and stability and allows us to obtain a very good qualitative agreement with the solutions reported in [34, 10, 18, 28, 29].

We now switch to the kEqn model. Figures 13, 14, and 15 display the time evolution of the potential temperature fluctuation computed with the kEqn model and meshes $h = 12.5, 25, 50$ m, respectively. We observe little difference between the solutions computed by the Smagorinsky model and the kEqn model with mesh $h = 50$ m for the entire duration of the time interval. Compare Figure 11 with Figure 15. The differences in the solutions given by the two LES models with mesh $h = 25$ m become visible around $t = 750$ s, when the largest recirculation given by the kEqn model has a more flattened top boundary. In addition, the quadri-rotor structure at $t = 900$ s given by the Smagorinsky model is more defined. Compare the bottom panels in 10 with Figure 14. The

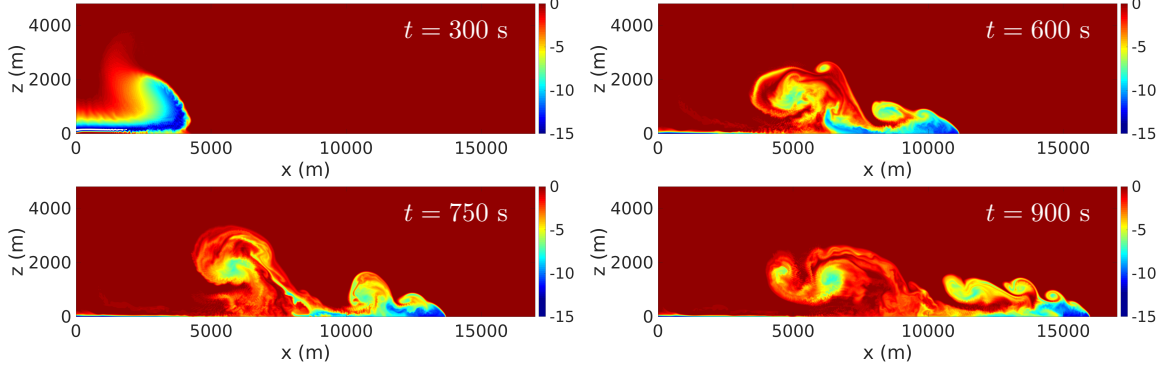


FIGURE 9. Density current, Smagorinsky model: time evolution of potential temperature fluctuation θ' computed with mesh $h = 12.5$ m.

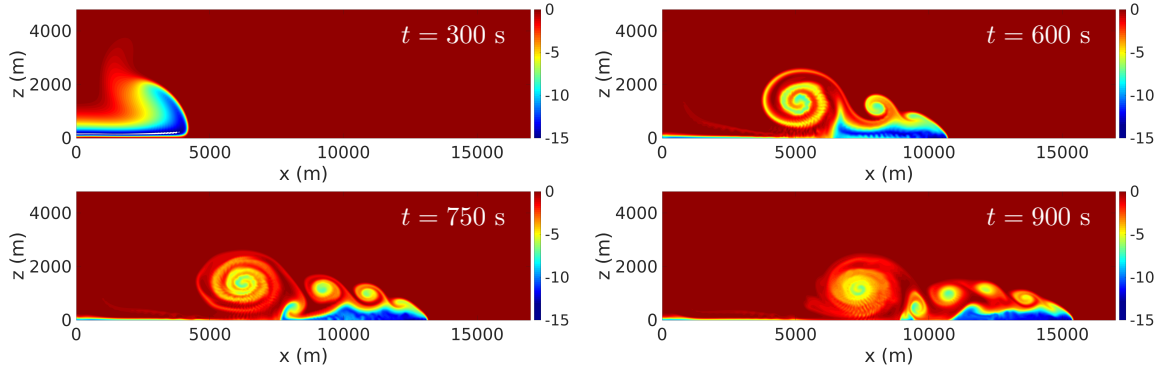


FIGURE 10. Density current, Smagorinsky model: time evolution of potential temperature fluctuation θ' computed with mesh $h = 25$ m.

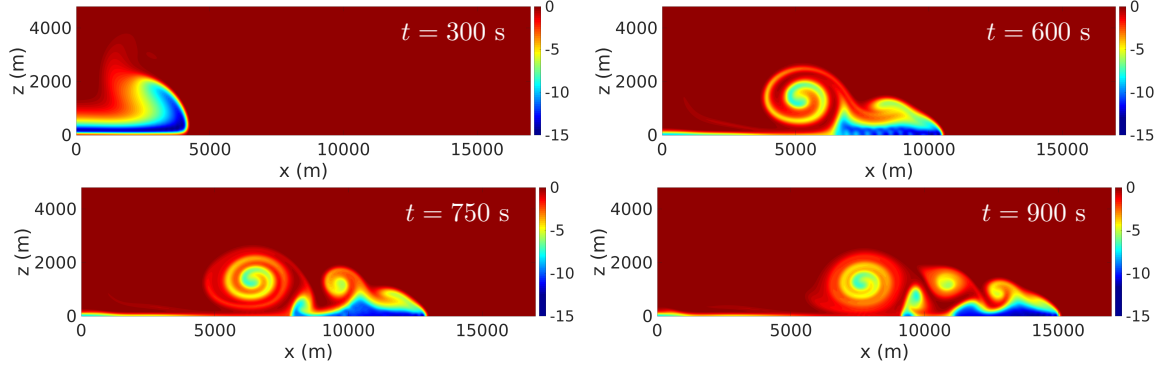


FIGURE 11. Density current, Smagorinsky model: time evolution of potential temperature fluctuation θ' computed with mesh $h = 50$ m.

differences in the solutions given the two LES models with mesh $h = 12.5$ m are pretty remarkable already at $t = 600$ s. Compare Figure 9 with Figure 13.

Figure 16 shows the time evolution of the space-averaged eddy viscosity (52) given by the kEqn model for meshes $h = 12.5, 25, 50$ m. By comparing Figure 16 with Figure 12, we observe that the two LES models have a very similar evolution of μ_{av} for mesh $h = 12.5$ m. For the other two meshes, the Smagorinsky model ramps up the value of μ_{av} faster than the kEqn model. Finally, we notice

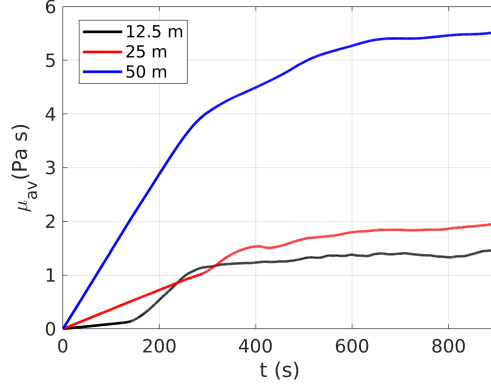


FIGURE 12. Density current, Smagorinsky model: time evolution of the average eddy viscosity (52) for meshes $h = 12.5, 25, 50$ m.

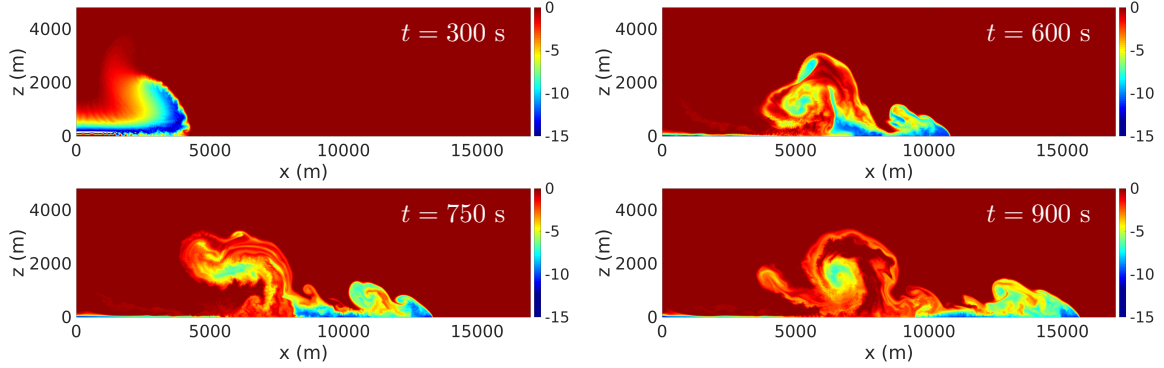


FIGURE 13. Density current, kEqn model: time evolution of potential temperature fluctuation θ' computed with mesh $h = 12.5$ m.

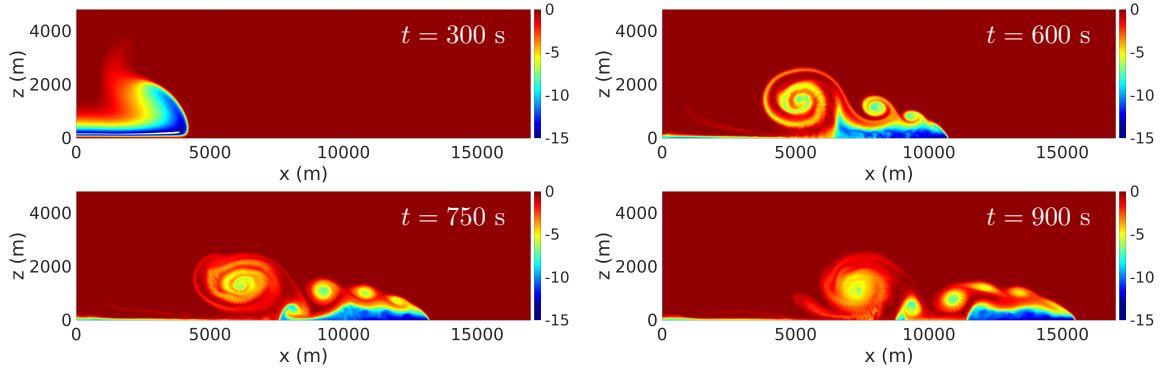


FIGURE 14. Density current, kEqn model: time evolution of potential temperature fluctuation θ' computed with mesh $h = 25$ m.

that the μ_{av} introduced by both models keeps increasing over the time interval $[0, 900]$ s since more and more vortical structures develop.

For a more quantitative comparison, we consider the front location, defined as the location on the ground where $\theta' = 1$ K, at $t = 900$ s. In Table 3, we report the space interval that contains the front location for our implementations of the AV75, Smagorinsky, and kEqn models. We compare our

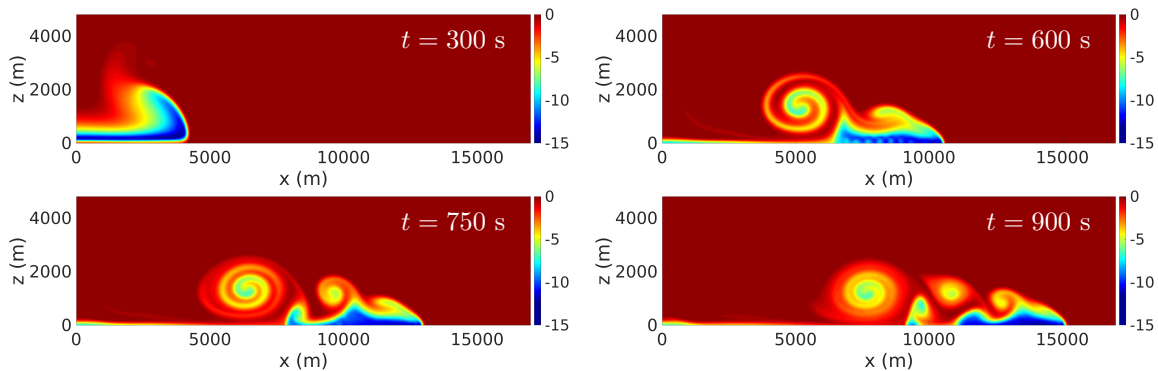


FIGURE 15. Density current, kEqn model: time evolution of potential temperature fluctuation θ' computed with mesh $h = 50$ m.

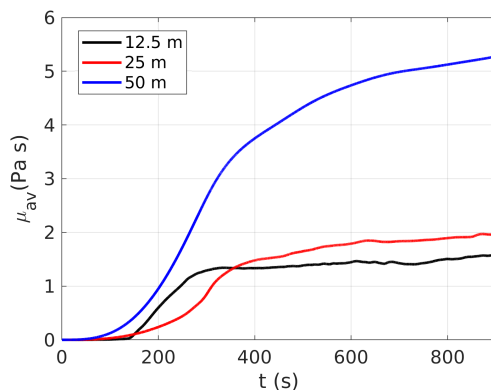


FIGURE 16. Density current, kEqn model: time evolution of the average eddy viscosity (52) for meshes $h = 12.5, 25, 50$ m.

values with the data in [34] (Table 4), which refer to the AV75 model and 14 different approaches for the numerical solution of this benchmark problem. We note that our results fall well within the values reported in [34]. Furthermore, from Table 3 we see that with our implementation of the Smagorinsky and kEqn models the front becomes faster as the mesh is refined. This is more evident with the Smagorinsky model than with the kEqn model, while the AV75 model shows the opposite trend. The front locations obtained with the AV75 model and different meshes are within about 500 m from each other. The same is true for the kEqn model, while the Smagorinsky model gives a larger variation in front location (about 900 m) as the mesh size varies. Since in [34] no results are reported for mesh $h = 12.5$ m, in Table 3 we list the front location found with a LES model and resolution 12.5 m in [29]. Such front location is within about 500 m of the value we obtain with the kEqn model and about 900 m of the value we get with the Smagorinsky model.

For a further quantitative comparison, we consider the potential temperature perturbation θ' at $t = 900$ s along the horizontal direction at a height of $z = 1200$ m. Figure 17 displays a comparison between the results given the AV75 model on meshes $h = 100, 50, 25$ m and the results obtained with the same model and resolution 25 m in [17]. Two numerical methods were used in [17] to approximate the solution: a spectral element method and a discontinuous Galerkin method, which provide curves that are superimposed in Figure 17 and are denoted as “Reference”. We observe that our results are slightly out of phase for meshes $h = 50, 100$ m with respect to the data in [17]. The potential temperature fluctuation obtained with mesh $h = 25$ m is in phase but has larger negative

Model	Resolution [m]	Front Location [m]
AV75	100	[15269, 15295]
AV75	50	[15141, 15167]
AV75	25	[14783, 14808]
Smagorinsky (LES)	50	[15104, 15130]
Smagorinsky (LES)	25	[15411, 15437]
Smagorinsky (LES)	12.5	[16000, 16026]
kEqn (LES)	50	[15181, 15206]
kEqn (LES)	25	[15514, 15539]
kEqn (LES)	12.5	[15642, 15667]
Ref. [34]	(25, 200)	(14533,17070)
Ref. [29]	12.5	15056

TABLE 3. Density current: our results for the front location at $t = 900$ s obtained with the AV75, Smagorinsky, and kEqn models and different meshes compared against results reported in [34, 29]. For reference [34], we reported the range of mesh sizes and front location values obtained with different methods. For reference [29], we report only the front location computed with the finest resolution.

peaks, especially in correspondence of the first recirculation. However, given all the differences between our approach and the one in [17], the comparison is satisfactory.

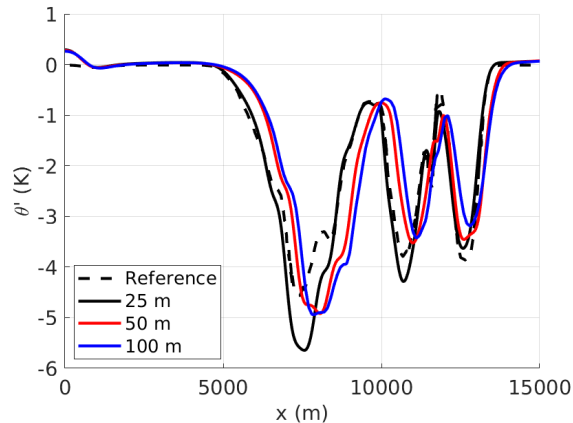


FIGURE 17. Density current: potential temperature perturbation θ' at $t = 900$ s along the horizontal direction at a height of $z = 1200$ m given the AV75 model on meshes $h = 100, 50, 25$ m and compared with data from [17] and resolution 25 m (denoted as “Reference”).

5. CONCLUDING REMARKS

The goal of this paper is to show that OpenFOAM provides a reliable and accurate framework for the simulation of non-hydrostatic atmospheric flows. To achieve this goal, we developed a pressure-based solver for the Euler equations written in conservative form using density, momentum, and total energy as variables and tested it against numerical data available in the literature for two well-known benchmarks, namely the rising thermal bubble and the density current. For the rising bubble and the density current tests, we obtain good qualitative and quantitative comparisons when the classical Smagorinsky model and/or the one equation eddy-viscosity model are adopted for stabilization. The code created for this paper is available within open source package GEA (Geophysical and Environmental Applications) [6].

ACKNOWLEDGEMENTS

We thank Dr. S. Marras for fruitful conversations. We acknowledge the support provided by the European Research Council Executive Agency by the Consolidator Grant project AROMA-CFD “Advanced Reduced Order Methods with Applications in Computational Fluid Dynamics” - GA 681447, H2020-ERC CoG 2015 AROMA-CFD, PI G. Rozza, and INdAM-GNCS 2019-2020 projects. This work was also partially supported by US National Science Foundation through grant DMS-1953535 (PI A. Quaini). A. Quaini acknowledges support from the Radcliffe Institute for Advanced Study at Harvard University where she has been the 2021-2022 William and Flora Hewlett Foundation Fellow.

REFERENCES

- [1] Atlas - A library for Numerical Weather Prediction and Climate Modelling. <https://sites.ecmwf.int/docs/atlas/>.
- [2] AtmosFOAM. <https://github.com/AtmosFOAM/AtmosFOAM>.
- [3] Climate Modeling Alliance. <https://github.com/CliMA>.
- [4] Community Earth System Model. <https://www.cesm.ucar.edu/>.
- [5] Energy Exascale Earth System Model. <https://e3sm.org/about/>.
- [6] GEA - Geophysical and Environmental Applications. <https://github.com/GEA-Geophysical-and-Environmental-Apps/GEA>.
- [7] Massachusetts Institute of Technology General Circulation Model. <http://mitgcm.org/>.
- [8] Weather Research and Forecasting. <https://www.mmm.ucar.edu/models/wrf>.
- [9] Horacio Aguerre, César Pairetti, Cesar Venier, Santiago Márquez Damián, and Norberto Nigro. An oscillation-free flow solver based on flux reconstruction. *Journal of Computational Physics*, 365:135–148, 2018.
- [10] N. Ahmad and J. Lindeman. Euler solutions using flux-based wave decomposition. *Int. J. Numer. Meth. Fluids*, 54:47–72, 2007.
- [11] N. N. Ahmad. High-resolution wave propagation method for stratified flows. In *AIAA Aviation Forum, Atlanta, GA*. AIAA, 2018.
- [12] M. Balogh, A. Parente, and C. Benocci. RANS simulation of ABL flow over complex terrains applying an Enhanced $k-\epsilon$ model and wall function formulation: Implementation and comparison for fluent and OpenFOAM. *Journal of Wind Engineering and Industrial Aerodynamics*, 104-106:360–368, 2012. 13th International Conference on Wind Engineering.
- [13] N. Botta, R. Klein, S. Langenberg, and S. Lutzenkirchen. Well balanced finite volume methods for nearly hydrostatic flows. *J. Comput. Phys.*, 196:539–565, 2004.
- [14] R. Carpenter, K. Droegemeier, P. Woodward, and C. Hane. Application of the piecewise parabolic method (PPM) to meteorological modeling. *Mon. Wea. Rev.*, 118:586–612, 1990.
- [15] Y. Feng, J. Miranda-Fuentes, J. Jacob, and P. Sagaut. Hybrid lattice boltzmann model for atmospheric flows under anelastic approximation. *Physics of Fluids*, 33(3):036607, 2021.
- [16] F. Flores, R. Garreaud, and R. C. Muñoz. CFD simulations of turbulent buoyant atmospheric flows over complex geometry: Solver development in OpenFOAM. *Computers & Fluids*, 82:1–13, 2013.
- [17] F. X. Giraldo and M. Restelli. A study of spectral element and discontinuous Galerkin methods for the Navier-Stokes equations in nonhydrostatic mesoscale atmospheric modeling: Equation sets and test cases. *J. Comput. Phys.*, 227:3849–3877, 2008.
- [18] F. X. Giraldo and M. Restelli. A study of spectral element and discontinuous Galerkin methods for the Navier-Stokes equations in nonhydrostatic mesoscale atmospheric modeling: Equation sets and test cases. *J. Comput. Phys.*, 227:3849–3877, 2008.
- [19] M. Girfoglio, A. Quaini, and G. Rozza. A Finite Volume approximation of the Navier-Stokes equations with nonlinear filtering stabilization. *Computers & Fluids*, 187:27–45, 2019.
- [20] Michele Girfoglio, Annalisa Quaini, and Gianluigi Rozza. A linear filter regularization for POD-based reduced order models of the quasi-geostrophic equations. <https://arxiv.org/abs/2211.16851>, 2022.
- [21] Michele Girfoglio, Annalisa Quaini, and Gianluigi Rozza. A novel large eddy simulation model for the quasi-geostrophic equations in a finite volume setting. *Journal of Computational and Applied Mathematics*, 418:114656, 2023.
- [22] N. Godinaud, P. Boivin, P. Freton, J-J. Gonzalez, and F. Camy-Peyret. Development of a new OpenFOAM solver for plasma cutting modeling. *Computers & Fluids*, 241:105479, 2022.
- [23] R. I. Issa. Solution of the implicitly discretised fluid flow equations by operator-splitting. *Journal of Computational Physics*, 62(1):40–65, 1986.
- [24] H. Jasak. *Error analysis and estimation for the finite volume method with applications to fluid flows*. PhD thesis, Imperial College, University of London, 1996.
- [25] J. F. Kelly and F. X. Giraldo. Continuous and discontinuous Galerkin methods for a scalable three-dimensional nonhydrostatic atmospheric model: limited-area mode. *J. Comput. Phys.*, 231:7988–8008, 2012.

- [26] G. Kristof, N. Racz, and M. Balogh. Adaptation of pressure based cfd solvers for mesoscale atmospheric problems. *Boundary-Layer Meteorol.*, 131:85–103, 2009.
- [27] G. Maragkos, S. Verma, A. Trouvé, and B. Merci. Evaluation of OpenFOAM’s discretization schemes used for the convective terms in the context of fire simulations. *Computers & Fluids*, 232:105208, 2022.
- [28] S. Marras, M. Moragues, M. Vázquez, O. Jorba, and G. Houzeaux. A Variational Multiscale Stabilized finite element method for the solution of the Euler equations of nonhydrostatic stratified flows. *J. Comput. Phys.*, 236:380–407, 2013.
- [29] S. Marras, M. Nazarov, and F. X. Giraldo. Stabilized high-order Galerkin methods based on a parameter-free dynamic SGS model for LES. *J. Comput. Phys.*, 301:77–101, 2015.
- [30] F. Moukalled, L. Mangani, and M. Darwish. *The Finite Volume Method in Computational Fluid Dynamics: An Advanced Introduction with OpenFOAM and Matlab*. 1st ed., Springer Publishing Company, Incorporated, 2015.
- [31] S. V. Patankar and D. B. Spalding. A calculation procedure for heat, mass and momentum transfer in three-dimensional parabolic flows. *International Journal of Heat and Mass Transfer*, 15(10):1787–1806, 1972.
- [32] V. Skurić, P. De Jaeger, and H. Jasak. Lubricated elastoplastic contact model for metal forming processes in OpenFOAM. *Computers & Fluids*, 172:226–240, 2018.
- [33] J. Smagorinsky. General circulation experiments with the primitive equations: I. the basic experiment. *Mon. Wea. Rev.*, 91:99–164, 1963.
- [34] J. Straka, R. Wilhelmson, L. Wicker, J. Anderson, and K. Droegemeier. Numerical solution of a nonlinear density current: a benchmark solution and comparisons. *Int. J. Num. Meth. in Fluids*, 17:1–22, 1993.
- [35] H. Weller, W. McIntyre, and D. Shipley. Multifluids for representing subgrid-scale convection. *Journal of Advances in Modeling Earth Systems*, 12(8):e2019MS001966, 2020.
- [36] H. G. Weller, G. Tabor, H. Jasak, and C. Fureby. A tensorial approach to computational continuum mechanics using object-oriented techniques. *Computers in physics*, 12(6):620–631, 1998.
- [37] H. Yamazaki, H. Weller, C. J. Cotter, and P. A. Browne. Conservation with moving meshes over orography. *Journal of Computational Physics*, 461:111217, 2022.
- [38] A. Yoshizawa and K. Horiuti. A statistically-derived subgrid-scale kinetic energy model for the large-eddy simulation of turbulent flows. *Journal of the Physical Society of Japan*, 54(8):2834–2839, 1985.